Effect of Reynolds number on amplitude branches of vortex-induced vibration of a cylinder

H. Jiao, G.X. Wu [a)]

Department of Mechanical Engineering, University College London, London WC1E 7JE, UK

Abstract

The effect of Reynolds number on curves of the transverse-only motion amplitude of a circular cylinder with the body mass $m^* = 0.935$ and the damping ratio $\zeta = 0.00502$ in the turbulent flow range is investigated systematically using a two-dimensional in-house code developed based on lattice Boltzmann method. Large eddy simulation is chosen as the turbulence model to describe viscous, incompressible and Newtonian fluid and the immersed boundary method is used to impose the boundary condition on the moving cylinder surface. Multi-block model is adopted to improve the accuracy and the computational efficiency. It is well established that when the variation of Reynolds number changes with the reduced velocity, there are three branches in the motion amplitude curve of a low mass cylinder, including initial, upper and lower branches connected by two jumps. However, in the present work, Reynolds number and reduced velocity are considered as independent parameters. Detailed results are provided for the variations of motion amplitude, motion frequency and lift coefficient against the reduced velocity in the lock-in region at different fixed Reynolds numbers. The results show that at a fixed Reynolds number the motion amplitude curve has two branches. At lower range of Reynolds number calculated, there are only initial and upper branches, and at higher range, there are only upper and lower branches. Also, the motion amplitude against the Reynolds number near the jumps is studied when the reduced velocity is fixed. It shows that the values of amplitude near the jumps are very sensitive to Reynolds number.

Keywords: vortex-induced vibration, motion amplitude branches, multi-block lattice Boltzmann method, immersed boundary method, large eddy simulation.

[a)] E-mail: g.wu@ucl.ac.uk

1. Introduction

Vortex-induced vibration (VIV) has been applied in many fields of engineering, such as rise tubes bringing oil or natural gas, the tethered structures in the ocean, the heat exchanger tubes, columns supporting bridges and high-rise buildings. Reviews of the earlier work were given by Bearman (1984), Blevins (1990) and Sumer and Fredsoe (1997) and more recent ones by Williamson and Govardhan (2004) and Bearman (2011). VIV may cause the large-amplitude vibration of structures and lead to structural damage or even collapse of the whole system, especially in the lock-in region. As a result, there have been a large number of experimental and numerical efforts to investigate features of the transverse free vibration in the lock-in region, including branches of motion amplitude, modes of vortex wake, the importance of body mass and damping. However, far fewer studies have systematically considered the effect of Reynolds number on the motion amplitude branches. Thus, this paper uses multi-block lattice Boltzmann method (LBM) together with large eddy simulation (LES) as the turbulence model for VIV. The immersed boundary method (IBM) is used to impose the no-slip condition on the body surface. The aim is to shed some lights on the effect of Reynolds number on free motions in the lock-in region, especially the motion amplitude branches.

Most previous experimental studies on the transverse free vibration of a cylinder in the sub-critical turbulent range (Reynolds number $Re = u_0 D/\nu = 300 - 2\times 10^5$) fixed structural parameters (the body mass m, structural stiffness k, damping b and diameter D) and the fluid medium (the fluid density ρ and kinematic viscosity ν), and varied the incoming fluid velocity u_0. In general, the response of the nondimensional cylinder motion amplitude $Y_0^* = \frac{Y_0}{D}$ depends on the nondimensional mass $m^* = \frac{m}{\rho D^2}$, damping ratio $\zeta = \frac{b}{2\sqrt{k(m+M_p)}}$, reduced velocity $U^* = \frac{u_0}{f_n D}$ and Reynolds number Re, where $M_p = \frac{\pi}{4}\rho D^2$ is the potential flow added mass for a circular cylinder and $f_n = \frac{1}{2\pi}\sqrt{\frac{k}{m+M_p}}$ is the natural frequency of the body. It means that in the experiment both U^* and Re could change with u_0. Then simulations tried to capture what was observed in experiments and thus followed the same practice. These early experimental and numerical studies assumed that the effect on the results was attributed to the variation of U^*

rather than the Reynolds number. A possible reason may be that in the sub-critical turbulence range, $f_v^* = f_v D/u_0$, where f_v is the frequency of lift coefficient C_L for a fixed cylinder, is found not to be too much affected by Re or to be nearly constant with a value of 0.2, as discussed in reviews by Williamson (1996) and Sumer and Fredsoe (1997). Also, the amplitude of C_L for a fixed cylinder was considered to be not very much affected by Re or to be nearly constant with a value of about 0.3 (Skop and Griffin, 1973; 1975). Then, the early assumption was that the amplitude of C_L would not be significantly affected by Re for a free body either. Therefore, as pointed out by Bearman (2011), "there was a popular belief at the time that Reynolds number plays a minor role and that the flow around a cylinder undergoing large vortex-induced vibrations is insensitive to Reynolds number changes".

Based on the more extensive work (Norberg, 2003; Klamo *et al.*, 2005; Govardhan and Williamson, 2006; Wanderley and Soares, 2015, Dorogi and Baranyi, 2020) undertaken later on, it is found that the effect of Re is important for various results, as reviewed by Bearman (2011). For example, Norberg (2003) reviewed data of the root-mean-square lift coefficient C_{Lrms} acting on a stationary cylinder in the sub-critical turbulent range. Results indicated that even though the value of C_{Lrms} was usually about 0.27, around $Re \approx 1600$ it suddenly dropped to 0.048. This suggested that the effect of Re on C_L for a fixed cylinder could not be always ignored. For a free body, the variation of C_L with Re should be more complex compared with that of a fixed cylinder, and thus the Re effect on free motions may need to be considered. Klamo *et al*. (2005) investigated the effect of Reynolds number in the range $Re = 525 - 2600$ on the maximum amplitude of a cylinder free motion. In their experiments, both U^* and Re still changed with the incoming fluid velocity u_0 at given m^* and ζ. A curve of motion amplitude Y_0^* against U^* was plotted between $U_1^* < U^* < U_2^*$,with $Re_1 < Re < Re_2$. Then, values of m^* and ζ remained unchanged, while f_n was varied. To achieve the same range U^*, u_0 was changed and therefore Re too. Another curve of motion amplitude Y_0^* against U^* between $U_1^* < U^* < U_2^*$, with $Re_3 < Re < Re_4$ was plotted. Comparing Y_0^* values from the two curves at same U^*, they found that at larger Re, the peak amplitude of the cylinder motion was also larger and pointed out that the Reynolds number was an important parameter for the maximum amplitude. Govardhan and Williamson (2006) extended the Re range to $500 - 33000$ to investigate its effect on the maximum motion amplitude and presented a similar conclusion to that from Klamo *et al*. (2005).

Later, Wanderley and Soares (2015) did numerical study. For given m^* and ζ, a curve of Y_0^* was plotted against U^* at a fixed Re. Curves Y_0^* at other Re values were also plotted against the same range of U^*. Similarly, curves for dominant frequency f_c^* of cylinder motion against U^* were plotted. In particular, four different Re values in the sub-critical turbulence range were chosen, or $Re = 300, 400, 1000$ and 1200. The body mass was $m^* = 1.88$ and damping ratio $\zeta = 0.00542$. It was found that the effect of Re was significant. With the increase in Re, the range of U^* within which lock-in occurred became much larger. In addition, at the same U^*, the value of motion amplitude from higher Reynolds number was higher than that from lower Reynolds number.

One of the important features of the motion amplitude curve of a low mass cylinder ($O(m^*) = 1 - 10$) against U^* is that it has jumps. Khalak and Williamson (1997) observed that for $O(m^*) = 1 - 10$, there were three branches of response in the curve. The curve started with an initial branch at lower U^*, then became an upper branch when U^* was beyond a critical value and dropped to a lower branch as U^* further increased to be beyond another critical value. Therefore, there are two jumps in the curve at: (1) the transition between initial-upper branches and (2) the transition between upper-lower branches. In the initial branch, with the increase of U^*, Y_0^* also increased. Further increase of U^* to a critical value U_{IU}^*, Y_0^* jumped nearly vertically from initial branch to the upper branch. The peak of the motion amplitude was located in the upper branch. As U^* continued to increase to the next critical value U_{UL}^*, the transition between upper-lower branches occurred, and Y_0^* dropped nearly vertically. It should be noted that in experiments mentioned above, U^* and Re both changed with u_0 and Re was in the range of 2000-14000. In the work of Wanderley and Soares (2015) mentioned previously, Re was fixed in the curve Y_0^* against U^* and was in the range $Re = 300 - 1200$. With the increase of U^*, Y_0^* increased slowly. Further increase in U^*, Y_0^* jumped to its peak first and then decreased. The curve changed rapidly before its peak, and thus there was only one critical value U_{IU}^* connecting initial and upper branches, no U_{UL}^* where Y_0^* dropped nearly vertically. It seems that the effect of Re on the response branches may be important and it may affect the response branches. We shall focus on the case with Re, within which the $Y_0^* - U^*$ curve has two jumps and three branches when the variation of Reynolds number changes with the reduced velocity. The range of Reynolds number is chosen as $Re = 1524 - 12192$ where Govardhan and

Williamson (2000) observed that there were three response branches and two jumps in the $Y_0^* - U^*$ curve when U^* and Re both changed with u_0. The large amplitude, including the peak response, and sudden changes of the motion amplitude may be found in the lock-in region, which may lead to the structural damage and have serious implications to the safety of the structure. Thus, it is important to investigate the characters of the motion in the lock-in region, especially response branches. We shall undertake systematic simulations to investigate how the $Y_0^* - U^*$ curve behaves at each fixed Re. In particular, we shall investigative how Re will affect both critical values, U_{IU}^* and U_{UL}^* at which the jump occurs and how it will affect the shape of the curve within each branch. Also, we shall examine how the motion amplitude changes near the jump when the reduced velocity is fixed while the Reynolds number varies. It ought to point out that in order to be consistent with amplitude branches from Govardhan and Williamson (2000), in the present paper a sudden increase is related to U_{IU}^* connecting initial and upper branches and a nearly vertical drop occurs at U_{UL}^* linking upper and lower branches. The results from Wanderley *et al.* (2012) indicated that the three-dimensionality had insignificant influence on the motion amplitude and frequency of a relatively long cylinder when Re ≤ 12000. Later, in addition to the work by Wanderley and Soares (2015), Pigazzini *et al.* (2018) extended Reynolds number to 13000. All of them provided the similar conclusion. Thus, 2D simulations are performed in the present study.

The present work on VIV is based on LBM. LBM is based on microscopic models and mesoscopic kinetic equations. Its equations may appear to be very different, but they are in fact equivalent to the NS equations. It has some distinctive features, such as the simple algorithm and the natural parallelism (Chen and Doolen, 1998). It can conveniently incorporate the LES model into its algorithm when turbulence is important and the LES-LBM can recover the incompressible LES-NS equations based on the Chapman-Enskog expansion (Cercignani, 1988) with the order of accuracy proportional to M^2, where $M = \frac{u_0}{c_s}$ is the Mach number, c_s is the equivalent sound speed (He and Luo, 1997). Macroscopic flow properties, such as the fluid density, velocity and pressure, can be obtained by the particle distribution function (Chen and Doolen, 1998). In this work, IBM is used to treat the structure-fluid boundary. The body surface is replaced by a layer of distributed force, whose value is determined by the no-slip boundary. It allows a complex boundary to be treated in a simpler way. To improve the numerical efficiency and accuracy, the multi-block grid method is used. The grid is finer near the fluid-structure boundary, where the flow is usually more complex, while it is coarser away from the body.

The paper is organized as follow. In Section 2, we present the numerical method based on immersed boundary-lattice Boltzmann method with large-eddy simulation and multi-block method for simulation of turbulence flows. This is followed by the mathematical analysis for the free motion in Section 3. Results are provided in Section 4, followed by the conclusions in Section 5.

2. Numerical method

Large-eddy simulation (LES) has become one of most widely used methods for turbulent flow. The turbulent flow of viscous, incompressible and Newtonian fluid is governed by the following continuity equation and Navier-Stokes equation with LES,

$$\nabla \cdot \bar{\boldsymbol{u}} = 0, \tag{1}$$

$$\frac{\partial \bar{\boldsymbol{u}}}{\partial t} + (\bar{\boldsymbol{u}} \cdot \nabla)\bar{\boldsymbol{u}} = -\frac{\nabla \bar{p}}{\rho} + 2\nu_0 \nabla \cdot \bar{\boldsymbol{S}} - \nabla \cdot \boldsymbol{T}, \tag{2}$$

where $\bar{\boldsymbol{u}}$ and $\bar{p}$ are filtered fluid velocity $\boldsymbol{u}$ and pressure p, respectively, ρ is the fluid density, ν_0 is the kinematic viscosity. $\bar{\boldsymbol{S}} = (\nabla\bar{\boldsymbol{u}} + (\nabla\bar{\boldsymbol{u}})^T)/2$ is the filtered strain rate tensor and $\boldsymbol{T}$ is sub-grid-scale stresses due to interaction between the unsolved or SGS eddies defined as $\boldsymbol{T} = \overline{\boldsymbol{u}\boldsymbol{u}} - \bar{\boldsymbol{u}}\bar{\boldsymbol{u}}$.

In one of the common LES models, or the sub-grid-scale (SGS) model due to Smagorinsky (1963), its aim is to reduce the temporal and spatial complexity of $\boldsymbol{T}$. It is assumed $\boldsymbol{T} = -2\nu_e\bar{\boldsymbol{S}}$, where $\nu_e = (C\Delta)^2\|\bar{\boldsymbol{S}}\|$ is eddy viscosity, C is the Smagorinsky constant and Δ is the filter width, $\|\bar{\boldsymbol{S}}\| = \sqrt{2\left|\sum_{\alpha,\beta}\bar{S}_{\alpha\beta}\bar{S}_{\alpha\beta}\right|}$ and $\bar{S}_{\alpha\beta} = \left(\frac{\partial \bar{u}_\alpha}{\partial x_\beta} + \frac{\partial \bar{u}_\beta}{\partial x_\alpha}\right)/2$, with $\alpha = 1,2$ and $\beta = 1,2$ corresponding to the lines and rows of $\bar{\boldsymbol{S}}$, respectively. Using this, Eq. (2) can be written as

$$\frac{\partial \bar{\boldsymbol{u}}}{\partial t} + (\bar{\boldsymbol{u}} \cdot \nabla)\bar{\boldsymbol{u}} = -\frac{\nabla \bar{p}}{\rho} + 2\nu_T \nabla \cdot \bar{\boldsymbol{S}}, \tag{3}$$

where $\nu_T = \nu_0 + \nu_e$ is the total viscosity. Eqs. (1) and (3) are then combined with the no-slip condition on the solid surface s, or

$$\bar{\boldsymbol{u}} = \boldsymbol{U}^d(s), \tag{4}$$

where $\boldsymbol{U}^d$ is the velocity of the solid surface.

2.1. Large-eddy simulation-lattice Boltzmann method (LES-LBM)

The present work is based on LBM with LES for governing equation in the volume coupled with IBM for conditions on the boundary. Equivalent to Eqs. (1) and (3), the lattice Boltzmann equation (LBE) with LES can be written as (Chen and Doolen, 1998; Aidun and Clausen, 2010)

$$f_i(\boldsymbol{x} + \boldsymbol{e}_i\delta_t, t + \delta_t) = f_i(\boldsymbol{x}, t) - \frac{1}{\tau_T}\left[f_i(\boldsymbol{x}, t) - f_i^{eq}(\boldsymbol{x}, t)\right], \tag{5}$$

where f_i is the weighted density distribution function corresponding to each discretized velocity $\boldsymbol{e}_i$, and f_i^{eq} is the corresponding equilibrium distribution function. $\boldsymbol{x}$ in Eq. (5) is the position vector in the Cartesian coordinate system Oxy and δ_t is the time step. $\tau_T = \frac{1}{2} + \frac{\nu_T}{c_s^2\delta_t}$ is the nondimensional total relaxation time, which is related to the total viscosity ν_T based on Chapman-Enskog expansion. Here c_s is the artificial sound speed. Based on SGS model, the relaxation time can be written as

$$\tau_T = \frac{1}{2} + \frac{1}{c_s^2\delta_t}(\nu_0 + \nu_e) = \frac{1}{2} + \frac{1}{c_s^2\delta_t}\left[\nu_0 + (C\Delta)^2\|\bar{\boldsymbol{S}}\|\right]. \tag{6}$$

For the two-dimension problem, we adopt the nine-discretized velocity, or D2Q9 model, as in the previous applications (Jiao and Wu, 2018a, b). Corresponding to that we have

$$\boldsymbol{e}_i = \begin{cases} (0,0) & i = 0 \\ c(\cos[(i-1)\pi/2], \sin[(i-1)\pi/2]) & i = 1-4, \\ \sqrt{2}c(\cos[(2i-1)\pi/4], \sin[(2i-1)\pi/4]) & i = 5-8 \end{cases} \tag{7}$$

where $c = \sqrt{3}c_s$ is the lattice speed. The equilibrium distribution function is of the form

$$f_i^{eq}(\boldsymbol{x}, t) = \rho\omega_i\left[1 + \frac{\boldsymbol{e}_i\cdot\bar{\boldsymbol{u}}}{c_s^2} + \frac{(\boldsymbol{e}_i\cdot\bar{\boldsymbol{u}})^2}{2c_s^4} - \frac{\bar{\boldsymbol{u}}\cdot\bar{\boldsymbol{u}}}{2c_s^2}\right], \tag{8}$$

where weighting coefficient ω_i are given as $\omega_0 = 4/9$, $\omega_i = 1/9$ for $i = 1-4$, and $\omega_i = 1/36$ for $i = 5-8$.

The fluid domain is then discretized by the structured mesh with $\delta_x = \delta_y = c\delta_t = l$. The solution of Eq. (5) is obtained through the streaming and collision process. From the density distribution function, the fluid density and the fluid velocity at each point can be respectively calculated as follow

$$\rho = \sum_{i=0}^{8} f_i, \tag{9}$$

$$\rho\overline{\boldsymbol{u}} = \sum_{i=0}^{8} \boldsymbol{e}_i f_i. \tag{10}$$

With the above LBM, Eq. (5) can be found to equivalent to Eqs. (1) and (3) to the order of accuracy of with $O(M^2)$ with $M = \frac{u_0}{c_s}$.

To find $\bar{S}_{\alpha\beta}$ required by the eddy viscosity in LES, there are at least two methods which could be conveniently used. The first one is to compute the velocity gradients using the finite-difference approximation, as square mesh will be used in the D2Q9 model. Another way is to evaluate it directly from the weighted density distribution function. In the present study, we have chosen the second method. In such a case, the strain rate tensor $\bar{S}_{\alpha\beta}$ is related to the momentum flux tensor $\bar{Q}_{\alpha\beta}$ detailed in Appendix, or

$$\bar{S}_{\alpha\beta} = -\frac{1}{2\tau_T\delta_t\rho c_s^2}\bar{Q}_{\alpha\beta} = \sum_i e_{i\alpha}e_{i\beta}\left(f_i - f_i^{eq}\right). \tag{11}$$

Substituting Eq. (11) into $\|\overline{\boldsymbol{S}}\| = \sqrt{2\left|\sum_{\alpha,\beta}\bar{S}_{\alpha\beta}\bar{S}_{\alpha\beta}\right|}$, we have $\|\overline{\boldsymbol{S}}\| = \frac{1}{2\tau_T\delta_t\rho c_s^2}\|\overline{\boldsymbol{Q}}\|$, where $\|\overline{\boldsymbol{Q}}\| = \sqrt{2\left|\sum_{\alpha,\beta}\bar{Q}_{\alpha\beta}\bar{Q}_{\alpha\beta}\right|}$. Combining this with Eq. (6) and eliminating τ_T, we obtain

$$\|\overline{\boldsymbol{S}}\| = \frac{c_s^2}{2C^2\Delta^2}\left(\sqrt{\tau_0^2\delta_t^2 + 2C^2\Delta^2\rho^{-1}c_s^{-4}\|\overline{\boldsymbol{Q}}\|} - \tau_0\delta_t\right) \tag{12}$$

and

$$\tau_T = \frac{1}{2} + \frac{1}{c_s^2\delta_t}\left[\nu_0 + \frac{c_s^2}{2}\left(\sqrt{\tau_0^2\delta_t^2 + 2C^2\Delta^2\rho^{-1}c_s^{-4}\|\overline{\boldsymbol{Q}}\|} - \tau_0\delta_t\right)\right], \tag{13}$$

where $\tau_0 = \frac{1}{2} + \frac{1}{c_s^2 \delta_t} \nu_0$ is related to the kinematic viscosity.

2.2. Multi-block model

The complexity level of the flow in different region is different. In order to improve the computational efficiency and accuracy of LES-LBM, the multi-block method (Yu *et al*., 2002) is used in the present study. This allows us to use finer grid in a region where flow changes more rapidly. To illustrate the procedure, a two-block system, with a coarser block and a finer block shown in Fig. 1, is considered. δ_x and δ_y are the space steps in x and y directions, respectively, and δ_t is the time step. The subscripts c and f indicate coarser and finer, respectively. Here we have $\delta_x = \delta_y = c\delta_t$, where c is the lattice speed. The ratio of the space steps between coarser and finer blocks (or the ratio of their corresponding time steps) is $m = \frac{\delta_{xc}}{\delta_{xf}} = \frac{\delta_{tc}}{\delta_{tf}}$. It should be noted that that the kinematic viscosity by ν_0 is the same in the two blocks. In this sense, τ_{0c} and τ_{0f} should be linked by the equation $\nu_0 = (\tau_{0c} - 0.5)c_s^2\delta_{tc} = (\tau_{0f} - 0.5)c_s^2\delta_{tf}$.

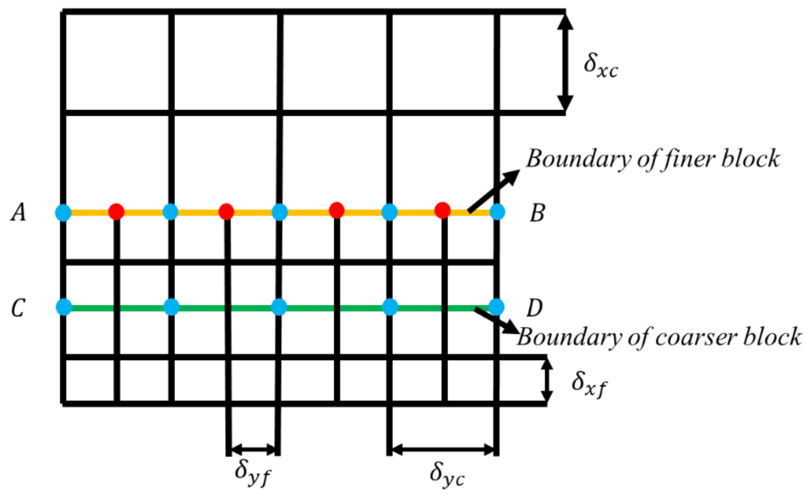

Fig. 1. Two blocks of different lattice spacing near their interface

The information exchange between two blocks on the interface is through interpolation. A cubic spline is used to eliminate the possibility of spatial asymmetry (Yu *et al*., 2002) caused by interpolation,

$$h(x) = a_i + b_i x + c_i x^2 + d_i x^3,\ x_{i-1} \le x \le x_i\ (i = 1, \cdots, n) \tag{14}$$

where x_i are the blue nodes along AB of the coarser block. Here $h_i = h(x_i)$ is known from the value of f in Eq. (5). The procedure to obtain coefficients a_i, b_i, c_i and d_i can be summarized as below.

(1) Approaching x_i within $x_{i-1} \le x \le x_i$, we can get the following equations

$$h_i = a_i + b_i x_i + c_i x_i^2 + d_i x_i^3, \tag{15}$$

$$h_i' = b_i + 2c_i x_i + 3d_i x_i^2, \tag{16}$$

$$h_i'' = 2c_i + 6d_i x_i. \tag{17}$$

(2) Similarly approaching x_i within $x_i \le x \le x_{i+1}$, we can have

$$h_i = a_{i+1} + b_{i+1} x_i + c_{i+1} x_i^2 + d_{i+1} x_i^3, \tag{18}$$

$$h_i' = b_{i+1} + 2c_{i+1} x_i + 3d_{i+1} x_i^2, \tag{19}$$

$$h_i'' = 2c_{i+1} + 6d_{i+1} x_i. \tag{20}$$

(3) Enforcing the continuities of the first and second derivatives at $x = x_i$, we can get

$$b_i + 2c_i x_i + 3d_i x_i^2 = b_{i+1} + 2c_{i+1} x_i + 3d_{i+1} x_i^2 \tag{21}$$

$$2c_i + 6d_i x_i = 2c_{i+1} + 6d_{i+1} x_i \tag{22}$$

Using these, together with in Eqs. (15) and (18), we have four equations at node i ($i = 1, \cdots, n-1$).

(4) At end nodes $i = 0$ and $i = n$, using known h_0 andh_n and also imposing zero second derivatives

$$2c_1 + 6d_1 x_0 = 0, \tag{23}$$

$$2c_n + 6d_n x_n = 0. \tag{24}$$

This will give 4 additional equations.

In total there are $4(n-1)+4=4n$ equations and the number is the same as that of the unknowns in Eq. (13). Thus, coefficients a_i, b_i, c_i and d_i $(i=1,\cdots,n)$ can be obtained. Then, from Eq. (13), we can calculate the values of $h(x)$ at the red points along AB of the finer block.

The finer grid also corresponds to smaller time step. Therefore, temporal interpolation is also needed. Let t_1, t_2 and t_3 be the time instants corresponding to the coarser grid. Based on the above spatial interpolation, the values at the finer grid nodes, or on both blue and red points of AB, at these time instants can be obtained. Let $g(t_1)$, $g(t_2)$ and $g(t_3)$ be at a given finer grid node. As a smaller time step δ_{tf} is used for the fine grid, result at t^* between the two instants is needed. Three-point Lagrangian formulation is then adopted for the temporal interpolation

$$g(t)=\sum_{k=1}^{3} g(t_k)\left(\prod_{j=1,j\neq k}^{3}\frac{t-t_j}{t_k-t_j}\right) \tag{25}$$

For t^*, we take one point t_3 on its right, and two points t_1 and t_2 on the left, as shown in Fig. 2, Eq. (25) may be expressed as

$$g(t^*)=g(t_1)\frac{(t^*-t_2)(t^*-t_3)}{(t_1-t_2)(t_1-t_3)}+g(t_2)\frac{(t^*-t_1)(t^*-t_3)}{(t_2-t_1)(t_2-t_3)}+g(t_3)\frac{(t^*-t_1)(t^*-t_2)}{(t_3-t_1)(t_3-t_2)} \tag{26}$$

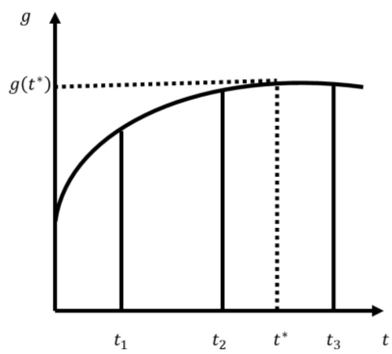

Fig. 2. Sketch for three-point Lagrangian interpolation

The relationship between t^* and t_2 is

$$t^*=t_2+j\delta_{tf}\ (j=1,\ldots,m-1). \tag{27}$$

Based on this equation and $t_3-t_2=t_2-t_1=\delta_{tc}=m\delta_{tf}$, Eq. (26) can be rewritten as

$$g(t^*) = \frac{j(j-m)}{2m^2} g(t_1) + \frac{j^2+m^2}{m^2} g(t_2) + \frac{j(j+m)}{2m^2} g(t_3). \tag{28}$$

For $m = 2$, we can have only $j = 1$ in Eq. (27)

$$t^* = t_2 + \delta_{tf}, \tag{29}$$

Eq. (28) becomes

$$g(t^*) = -0.125g(t_1) + 0.75g(t_2) + 0.375g(t_3). \tag{30}$$

For $m = 2$, the detailed exchange between the finer and coarser blocks is summarized as follow.

(1) $f_i(\boldsymbol{x}, t + 2\delta_{tf})$ in the coarser block can be calculated by collision and streaming of $f_i(\boldsymbol{x}, t)$ as in Jiao and Wu (2018a), which provides its values along the blue points of AB;

(2) $f_i(\boldsymbol{x}, t + 2\delta_{tf})$ of red points on the AB line for the finer block can be calculated by Eq. (14).

(3) $f_i(\boldsymbol{x}, t + \delta_{tf})$ in the finer block can be calculated by collision and streaming of $f_i(\boldsymbol{x}, t)$;

(4) The values of $f_i(\boldsymbol{x}, t + \delta_{tf})$ at both blue and red points of AB are obtained from Eq. (30), which are used as the boundary condition for the finer block

(5) $f_i(\boldsymbol{x}, t + 2\delta_{tf})$ in the finer block can be calculated by collision and streaming of $f_i(\boldsymbol{x}, t + \delta_{tf})$ with the boundary condition along AB;

(6) $f_i(\boldsymbol{x}, t + 2\delta_{tf})$ values on the blue points along CD line obtained from the finer mesh is used as boundary condition for the coarser;

(7) Return to step (1) and start the next time.

2.3. Immersed boundary method

The present work uses IBM for boundary condition, which imposes no-slip condition on the structure-fluid boundary by replacing the body surface with a layer of distributed force $\boldsymbol{g}$ into Eq. (3). To combine this IBM with the present LES-LBM, Eq. (5) can be modified as

$$f_i(\boldsymbol{x} + \boldsymbol{e}_i\delta_t, t + \delta_t) = f_i(\boldsymbol{x}, t) - \frac{1}{\tau_T}\left[f_i(\boldsymbol{x}, t) - f_i^{eq}(\boldsymbol{x}, t)\right] + \delta_t \frac{\omega_i \rho}{c_s^2} \boldsymbol{e}_i \cdot \boldsymbol{g}. \tag{31}$$

The detailed process to obtain $\boldsymbol{g}$ can be found in Jiao and Wu (2018a). The value of the external force $\boldsymbol{g}$ is obtained by the delta function δ_l

$$\boldsymbol{g}(\boldsymbol{x},t) = \sum_s \boldsymbol{G}(s,t)\delta_l\big(\boldsymbol{x} - \boldsymbol{X}(s,t)\big),$$

where $\boldsymbol{X}(s,t)$ is the position of the body surface and will change with time when the body is in motion. The required body force on the solid boundary is to ensure the no-slip condition through the proper choice of the forcing term, which is given as

$$\boldsymbol{G}(s,t) = \frac{\boldsymbol{U}^d(s,t) - \boldsymbol{U}^*(s,t)}{\delta_t}.$$

Here $\boldsymbol{U}^*$ is the velocity on the boundary without the forcing term. It is obtained from

$$\boldsymbol{U}^*(s,t) = \sum_{\vec{x}} \boldsymbol{u}^*(\vec{x},t)\delta_l\big(\boldsymbol{x} - \boldsymbol{X}(s,t)\big),$$

where $\boldsymbol{u}^*$ is the fluid velocity without the forcing term from Eq. (3). Based on Peskin (2002), the delta function $\delta_l(\boldsymbol{x})$ can be written as follow

$$\delta_l(\boldsymbol{x}) = \delta_l(x)\delta_l(y),$$

where

$$\delta_l(r) = \begin{cases} \frac{1}{4l}\left[1 + \cos\left(\frac{\pi|r|}{2l}\right)\right] & |r| \le 2l \\ 0 & otherwise \end{cases}.$$

Here l is the grid size of the fluid domain.

3. Free motion of a body

The fluid force on the cylinder is calculated by integrating the external force $\boldsymbol{g}(\boldsymbol{x},t) = \big(g_x(\boldsymbol{x},t), g_y(\boldsymbol{x},t)\big)$ over the whole fluid domain. The drag and lift forces are given by

$$F_D = \iint g_x(\boldsymbol{x},t)dxdy \tag{32}$$

and

$$F_L = \iint g_y(\boldsymbol{x},t)dxdy. \tag{33}$$

In reality, this integration needs to be performed only over the layer next the body surface because of the delta function $\delta_l(\boldsymbol{x})$. The corresponding coefficients are defined by $C_D = F_D/0.5\rho u_0^2 D$ and $C_L = F_L/0.5\rho u_0^2 D$, respectively.

In many engineering problems, the transverse motion of the body or the motion in the *y* direction due to flow in *x* direction is the main concern, because the lift (transverse) fluctuation is generally much larger than drag (in-line) fluctuation. If the body mass is m, the structural damping is b and stiffness is k, the governing equation of its motion is

$$m\ddot{Y} + b\dot{Y} + kY = F_L, \tag{34}$$

where Y is the displacement, and the over dot denotes the temporal derivative.

The nondimensionalized form of Eq. (34) based on ρ, u_0 and D can be written as

$$m^*\ddot{Y}^* + \frac{4\pi\zeta(m^*+M_p^*)}{U^*}\dot{Y}^* + \frac{4\pi^2(m^*+M_p^*)}{U^{*2}}Y^* = \frac{C_L}{2}, \tag{35}$$

where $M_p^* = \frac{\pi}{4}$ is the nondimensionalized potential flow added mass.

For a fixed cylinder, $Y^* = 0$. C_L will be only a function of Reynolds number including its amplitude C_{L0} and frequency f_v^*, or

$$C_L = C_L(Re), \tag{36}$$

$$C_{L0} = C_{L0}(Re), \tag{37}$$

$$f_v^* = f_v^*(Re). \tag{38}$$

As discussed in the Introduction, in the sub-critical range ($Re = 300 - 2 \times 10^5$), f_v^* is almost constant with a value of 0.2 (Williamson, 1996; Sumer and Fredsoe, 1997), and so C_{L0} is, which is around 0.3 (Skop and Griffin, 1973; 1975), apart from the drop around $Re \approx 1600$ (Norberg, 2003).

For a cylinder in oscillation, one can expect that C_L may be affected by the motion amplitude Y_0^* and motion frequency f_c^*. Thus, Eq. (35) becomes

$$C_L = C_L(Y_0^*, f_c^*, Re). \quad (39)$$

According to Eq. (35), Y^* depends on the body mass, damping ratio, reduced velocity and lift coefficient, or

$$Y^* = Y^*(m^*, \zeta, U^*, C_L). \quad (40)$$

It is then obvious there is some nonlinear interaction between C_L and Y^*. In such a case, unlike that for a fixed cylinder in Eq. (36), C_L in Eq. (39) for a cylinder in oscillation may be more sensitive to Re. This will be investigated through extensive simulations below.

4. Results

4.1. Verification through comparison

4.1.1. Cavity

The driven square cavity flow at $Re = 1000 - 5000$ has been carried out first to verify the numerical method. The initial and boundary conditions are the same as those used by Hou *et al*. (1996). The cavity has 256 lattice units on each side. Initially, the velocities at all nodes, except the top, are set to zero. At the top, the *x*-velocity of the top is u_0 and the *y*-velocity is zero. and no-slip boundary conditions are used at the three stationary walls. Values of the Mach number M and the Smagorinsky constant C are also the same as those used by Hou *et al*. (1996), or $M = 0.17$ and $C = 0.1$.

Table 1 shows the comparison of results for the strength and location of the primary vortex, lower left vortex and lower right vortex at $Re = 1000$. Figures 3 - 4 display comparison of streamline and vortex contours at $Re = 5000$, respectively. There is an excellent agreement between present results and those published previously, suggesting that the present numerical method is correct and results are accurate.

Table 1

Comparison of results for primary vortex, lower left vortex and lower right vortex at $Re = 1000$

	Primary vortex		Lower left vortex	Lower right vortex
Reference	Strength	Location	Location	Location
Present	2.0550	(0.5335, 0.5671)	(0.0875, 0.0813)	(0.8643, 0.1180)
Hou *et al.* (1995)	2.0760	(0.5333, 0.5647)	(0.0902, 0.0784)	(0.8667, 0.1137)
Chen (2009)	-	(0.5310, 0.5700)	(0.0901, 0.0800)	(0.8501, 0.1100)
Ghia *et al.* (1982)	2.04968	(0.5313, 0.5625)	(0.0859, 0.0781)	(0.8594, 0.1094)

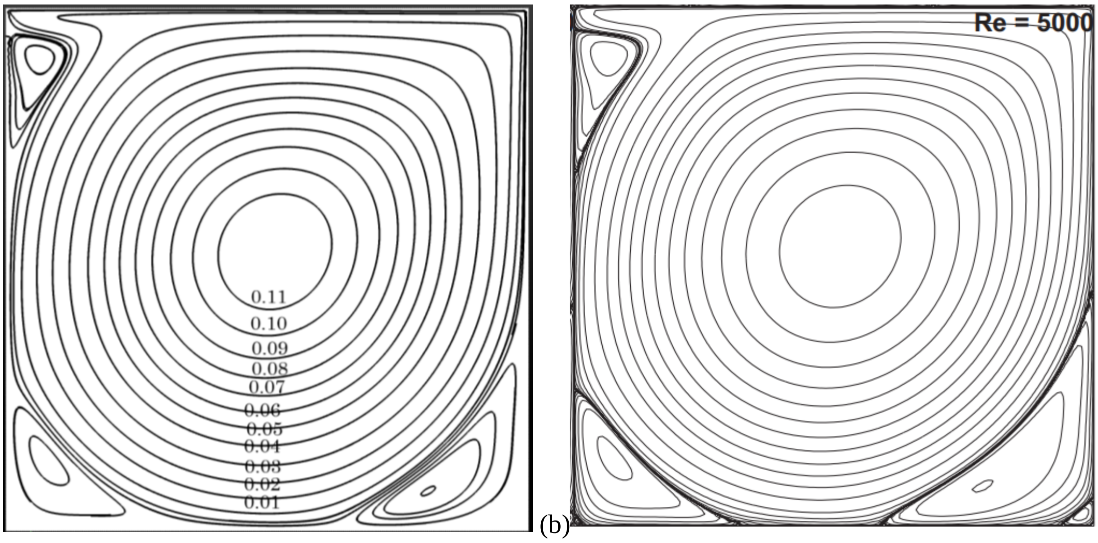

Fig. 3. Streamlines at $T = 185$ and $Re = 5000$: (a) present and (b) Garcia (2007).

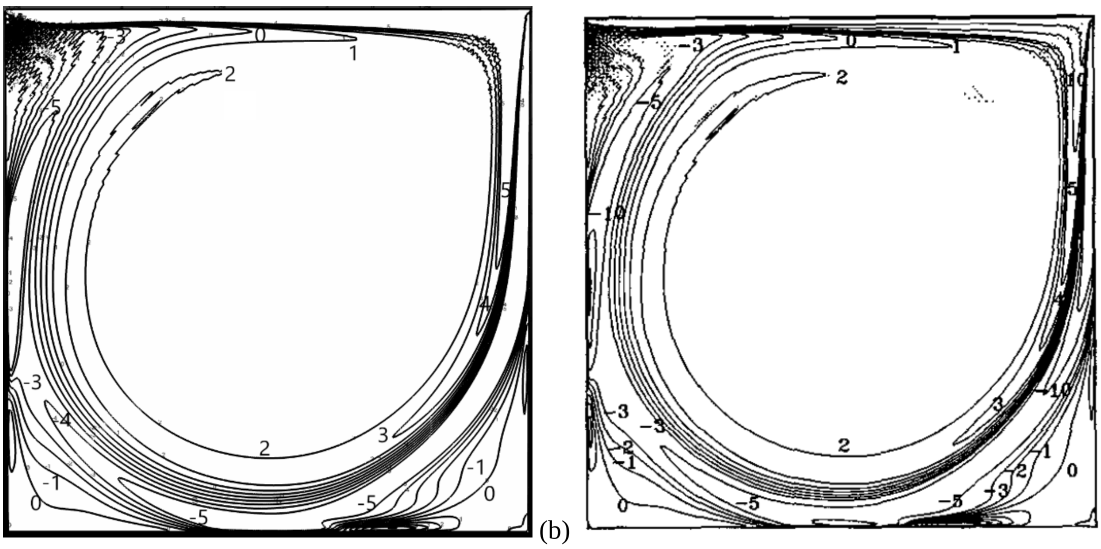

Fig. 4. Vortex contours at $T = 185$ and $Re = 5000$: (a) present and (b) Hou (1996).

4.1.2. Free motion of a cylinder

A sketch of the computational domain for free motions of a circular cylinder with diameter D is shown in Fig. 5(a). The same domain is used in the rest of this work. The incoming flow is from the left-hand side of the body. The cylinder is located in the flow field. $Le = 22D$, $Ls = 5D$ and $Lr = 40D$, which is similar to that used by Pigazzini *et al.* (2018). A Dirichlet boundary condition ($\vec{u} = (u_0, 0)$) is adopted at the inflow and outlet boundaries. $p = c_s^2$ is adopted at the inflow and outlet boundaries. On the upper and lower boundaries, y-velocity and the component of stress vector along these two boundaries are prescribed zero value. Initially, the velocities at all nodes, except inflow and outlet boundaries, are set to zero. There are three levels of grids in the calculation shown in Fig. 5(b). The ratio of space steps between Grid 2 and Grid 1 is 2 and the ratio between Grid 3 and Grid 1 is 4. The grid parameter in Grid 1 is $s = D/\delta_x = 400$. The ratio between the arc length (δ_s) of the boundary element and the structured mesh (δ_x) in Grid 1 is $\delta_{sx} = \frac{\delta_s}{\delta_x} = 1.67$, which is similar to that of the minimum value adopted in Chen et al. (2018). The Mach number is taken as $M = 0.02$. Yu et al. (2005) indicated that in LES-LBM, the value of the Smagorinsky constant $C = 0.1$ yielded better results than the value of $C = 0.17$ which is always used in LES-NS, and thus $C = 0.1$ is used in the present study. For analyses, the fluctuating force history is collected for a sufficiently long period of time ($T = u_0 t/D > 1200$).

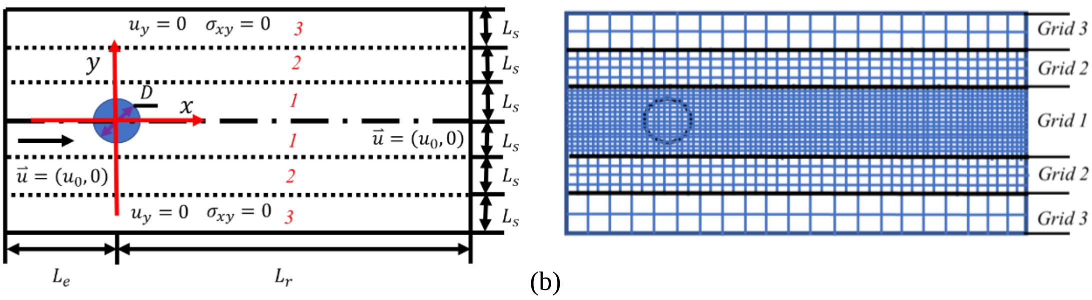

Fig. 5. (a) Computational configuration and (b) schematic diagram of grid levels

To further validate our method, we compare our numerical results with the experimental data from Govardhan and Williamson (2000) for a cylinder in free motion. In such a case, body mass is taken as $m^* = 0.935$ and accordingly damping ratio as $\zeta = 0.00502$. The reduced velocity U^* varies from 3 to 24 and corresponding Reynolds number from 1524 to 12192. It is found in our simulations that lock-in where the dominant frequency of the lift coefficient is equal to that of cylinder motion occurs in the region of $U^* = 3.5 - 17.5$, which is similar to that in Govardhan and Williamson (2000). Spectra of cylinder motion and lift coefficient in the lock-in region are not purely sinusoidal, but still discrete, which is the same as that in Pigazzini *et al.* (2018). In addition to the dominant frequency component, there are multiple intricate frequencies in spectra. It should be noted that in in Jiao and Wu (2018b) and Kumar *et al.*(2016), the system can be regarded as the state of the lock-in when (a) the dominant frequency in the power spectrum of the lift coefficient is equal to the forced oscillation frequency f_c and (b) other components in its power spectrum, if any, are only at integer multiples of f_c. Compared with that mentioned in Jiao and Wu (2018b) and Kumar *et al.* (2016), the definition of lock-in here has been extended to account for the turbulent flow effect on the result. Figure 6 shows motion amplitude Y_0^* and frequency ratio $f^* = f_c^*/f_n^*$ in the lock-in region, where f_c^* is the dominant frequency of the cylinder motion. It can be seen that in the Y_0^* curve, there are two jumps and three amplitude branches, including initial ($3.5 \leq U^* \leq U_{IU}^*$), upper ($U_{IU}^* < U^* \leq U_{UL}^*$) and lower branches ($U_{UL}^* < U^* \leq 17.5$), as defined by Khalak and Williamson (1997). In the initial branch, with the increase of U^*, Y_0^* also increases. Further increase of U^* to U_{IU}^*, Y_0^* jumps nearly vertically from initial value to the upper branch within which the peak of the motion amplitude $Y_{0max}^* = 0.91$ is located at $U^* = 8.0$ ($Re = 4064$). As U^* continues to increase to U_{UL}^*, the transition between upper-lower branches occurs, and Y_0^* drops nearly vertically. In the present study with smaller incremental increase of U^* than that from Govardhan and Williamson (2000), U_{IU}^* is found to be in the range from 5.0 to 5.1, and U_{UL}^* from 10.5 to 10.6. Figure 7 shows displacement and lift coefficient histories at U_{IU}^* and U_{UL}^*. At the lower end of U_{IU}^*, lift coefficient and displacement are almost in phase, while at the higher end of U_{UL}^*, they become nearly anti-phase. These phenomena are consistent with that observed in the experiment by Govardhan and Williamson (2000). The result in Fig. 6 are generally in good agreement with those from Govardhan and Williamson (2000), although the peak of the motion amplitude $Y_{0max}^* = 0.91$ at $U^* = 0.75$ is a bit smaller than $Y_{0max}^* = 1.01$ in Govardhan and Williamson (2000). Figure 8 shows the amplitude C_{L0} of lift coefficient in the lock-in region. It can be seen that when $U^* = U_{UL}^*$, there is also a sudden drop in C_{L0}, about from 0.70 to 0.37.

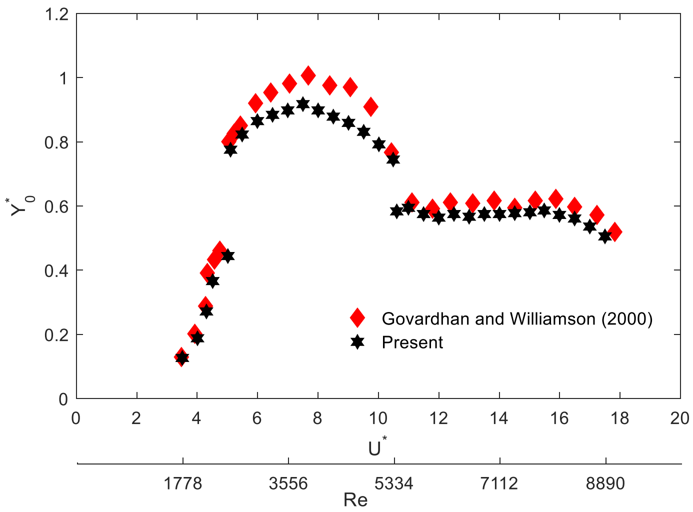

(a)

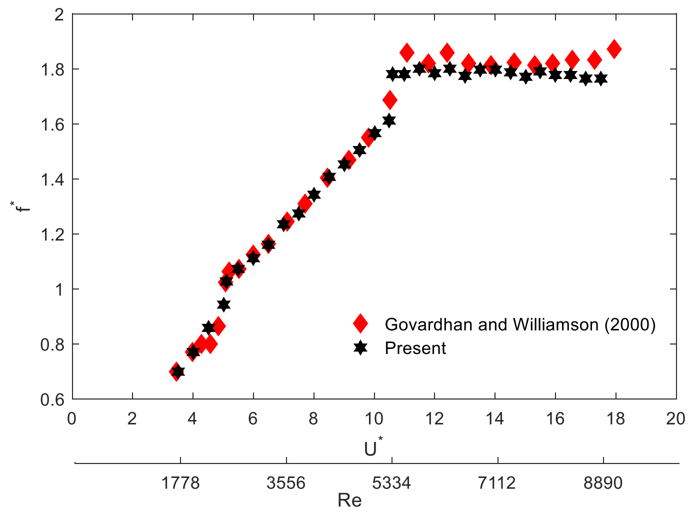

(b)

Fig. 6. Comparison of motion amplitude and frequency ratio between experimental data from Govardhan and Williamson (2000) and present results.

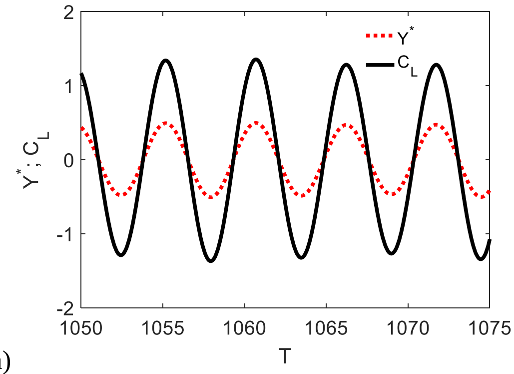

(a)

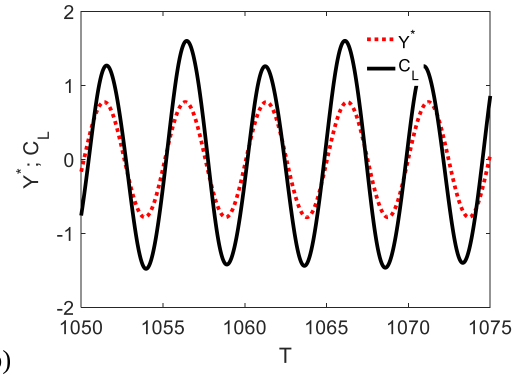

(b)

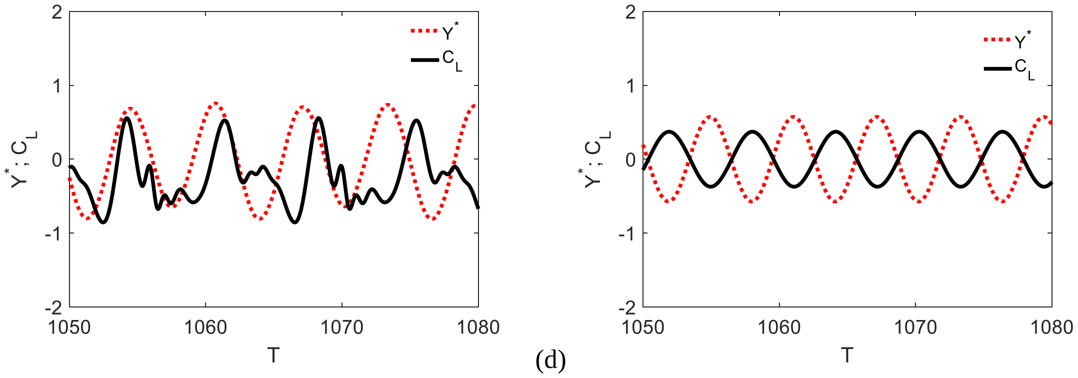

(c) (d)

Fig. 7. Displacement and lift coefficient near critical reduced velocity between initial and upper branches ((a),(b), and near that between upper and lower branches ((c), (d)) (a) $U^* = 5.0$ ($Re = 2540$), (b) $U^* = 5.1$ ($Re = 2590$), (c) $U^* = 10.5$ ($Re = 5334$) and (d) $U^* = 10.6$ ($Re = 5385$).

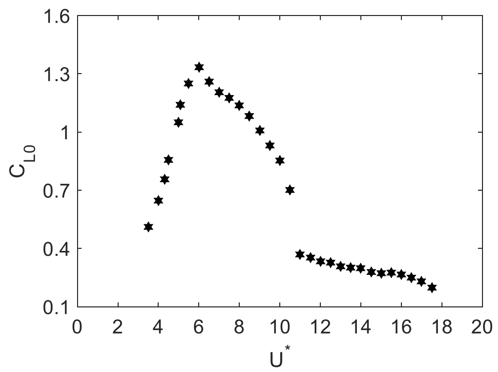

Fig. 8. Amplitude of lift coefficient.

4.2. Variation of body motion with reduced velocities at different fixed Reynolds numbers

If we assume

$$C_L = C_{L0} sin(2\pi f_c^* T + \phi) \text{ or } C_L = \text{Re}\left[iC_{L0}e^{-i(2\pi f_c^* T + \phi)}\right], \tag{41}$$

and the motion of the cylinder can then be written as

$$Y^* = Y_0^* sin(2\pi f_c^* T) \text{ or } Y^* = \text{Re}\left[iY_0^* e^{-i(2\pi f_c^* T)}\right], \tag{42}$$

where ϕ is the phase angle between the lift coefficient and cylinder motion, we can have

$$Y_0^* = \frac{U^{*2}}{8\pi^2}\sqrt{\frac{1}{\left[(m^*+M_p^*)-m^* f^{*2}\right]^2 + 4\zeta^2\left(m^*+M_p^*\right)^2 f^{*2}}}\, C_{L0}. \tag{43}$$

In the following computations of this section, we may fix m^* and ζ, as well as Re, and vary only U^*. Equation (43) shows that Y_0^* will be directly affected by the term of U^*. It will also be affected implicitly by f^* which will change with U^*. When Y_0^* and f^* change with U^*, C_{L0}

will also change, which further affects Y_0^*. Therefore, there is a complex nonlinear interaction. The process of interaction will be different when Re is different. We shall undertake extensive simulations to have a better understanding of the force and motion behaviour. To investigate the effects of Reynolds number Re and reduced velocity U^* individually, Re changes with kinematic viscosity ν and U^* with natural frequency f_n in the following simulations.

We first choose $Re = 1778$ which is the low end of lock-in region in the previous case shown in Fig. 6, and simulations have been undertaken for reduced velocity in the range of $U^* = 3.5 - 17.5$. It is found that lock-in occurs at $U^* \leq 12.0$. Figure 9 shows (a) the motion amplitude Y_0^* and (b) frequency ratio f^* in the lock-in region. Within the range of $U^* = 3.5 - 12.0$, the variation of the frequency ratio f^* is from 0.70 to 1.31. For this Reynolds number $Re = 1778$, $Y_{0max}^* = 0.59$ at $U^* \approx 6.0$ is the peak of motion amplitude in the lock-in region. It can be seen that the motion amplitude Y_0^* changes rapidly before its peak similar to that from Wanderley and Soares (2015), and two sides of the peak correspond to the initial and upper branches. With the increase of U^*, the motion amplitude Y_0^* in the initial branch also increases while Y_0^* in the upper branch has the opposite trend. This may be partly explained by amplitude C_{L0} of lift coefficient in Fig. 10. It can be seen that the shape of the Y_0^* curve is the similar to that of C_{L0}. When U^* increases, C_{L0} increases slowly first and then jumps to its peak value at $U^* \approx 6.0$, where Y_{0max}^* occurs. As U^* continues to increase, C_{L0} decreases.

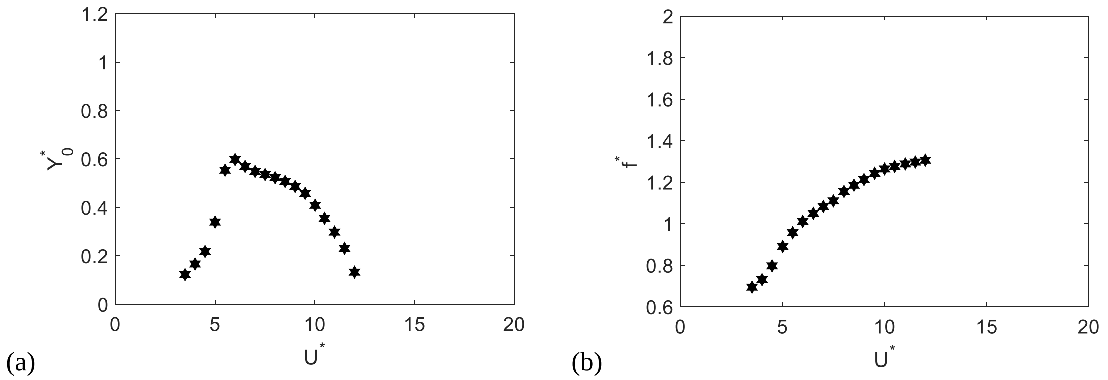

Fig. 9. Motion amplitude and frequency ratio at $Re = 1778$.

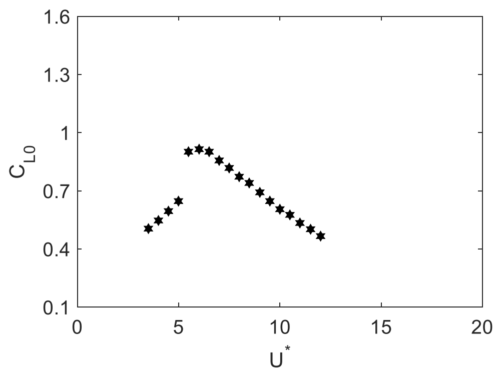

Fig. 10. Amplitude of lift coefficient at $Re = 1778$.

When $Re = 3556$, simulations were made in the range of $U^* = 3.5 - 17.5$. It is found that here lock-in occurs when $U^* \leq 13.0$, whose range is larger than that in the previous case of $Re = 1778$. Figure 11 shows the motion amplitude Y_0^* and frequency ratio f^* in the lock-in region. The peak $Y_{0max}^* = 0.89$ at $Re = 3556$ is much larger than $Y_{0max}^* = 0.59$ at $Re = 1778$ in Fig. 9. It seems that with the increase of Re, the value of the peak Y_{0max}^* also increases, which was also observed in Klamo *et al.* (2005) and Govardhan and Williamson (2006), whose work focused only on the effect of Re on Y_{0max}^*. In addition, for $Re = 3556$, the free motions against reduced velocity are very different from that in the previous cases in Fig. 9. Here, with the increase of U^*, Y_0^* also increases first. At $U^* \approx 5.0 - 6.0$, it increases rapidly and at $U^* \approx 7.0$, it reaches its peak value in the lock-in region. The motion amplitude Y_0^* drops steeply after its peak, while it drops smoothly at $Re = 1778$. As U^* further increases, Y_0^* still decreases. It means that there is a critical value U_{UL}^* which connects the upper and lower branches, instead of U_{IU}^* in the previous case. At $Re = 3556$, the sudden drop at U_{UL}^* is similar to that in Fig. 6. But here the drop occurs at the peak, while in Fig. 6 it is away from the peak location. There is a rapid variation of Y_0^* before its peak. However, this is not like the almost vertical jump in Figs. 6 and 9 before Y_0^* arrives to its peak. Figure 12 shows the amplitude of lift coefficient in the lock-in region. It can be seen that the shape of the Y_0^* curve may be similar to that of C_{L0} in the lock-in region, which is also found at $Re = 1778$ in Fig. 10.

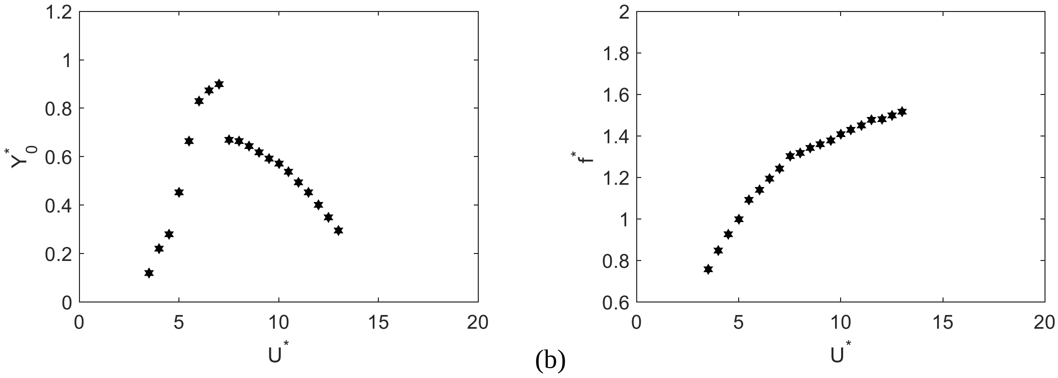

(a) (b)

Fig. 11. Motion amplitude and frequency ratio at $Re = 3556$.

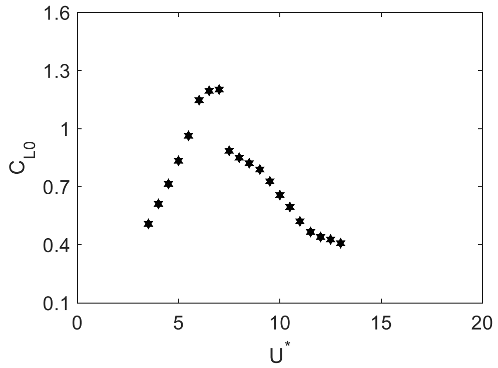

Fig. 12. Amplitude of lift coefficient at $Re = 3556$.

Simulations at $Re = 5334$ have been carried out in the range of $U^* = 3.5 - 17.5$. It is found that when Reynolds number is fixed at $Re = 5334$, lock-in occurs when $U^* \leq 15.0$, whose range is larger than that in the previous two cases of $Re = 1778$ and 3556. Figure 13 shows the motion amplitude Y_0^* and frequency ratio f^* in the lock-in region. At $U^* = 8.0$, $Y_{0max}^* = 0.92$ is the peak of motion amplitude in the lock-in region. Compared with the two previous cases at $Re = 1778$ and 3556, there is an increase in the value of reduced velocity where the peak Y_{0max}^* occurs. At $Re = 5334$, there is still a critical value, U_{UL}^* where Y_0^* drops nearly vertically from upper branch to lower branch, similar to that in the previous case of $Re = 3556$. The drop at $U_{UL}^* = 10.5 - 10.6$ does not occur at the peak, which is similar to that in Fig. 6 and is different from that in Figs. 9 and 11. Figure 14 shows the amplitude of lift coefficient in the lock-in region. Here, the peak of C_{L0} is at $U^* \approx 7.0$ smaller than $U^* = 8.0$ where Y_{0max}^* occurs, which is different from that in $Re = 1778$ and 3556. It may be because within about the range of $U^* = 7.0 - 8.0$, the amplitudes of C_L at more frequency components become visible and significant, even though the C_L history is still periodic with respect to time.

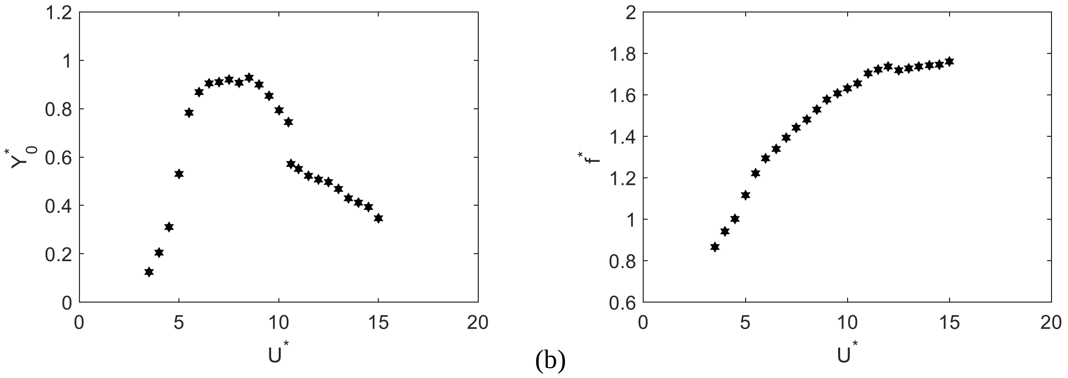

(a) (b)

Fig. 13. Motion amplitude and frequency ratio at $Re = 5334$.

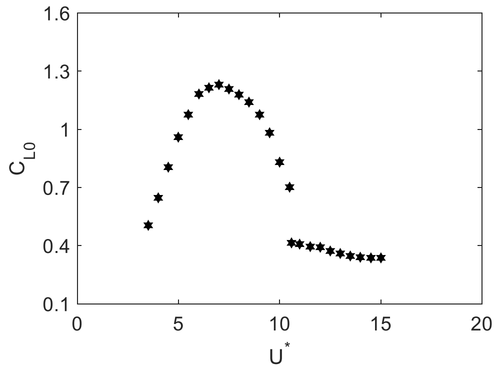

Fig. 14. Amplitude of lift coefficient at $Re = 5334$.

We also provide the case in the range of $U^* = 3.5 - 17.5$ at $Re = 8890$ which is the high end of lock-in region in the previous case shown in Fig. 6. At this Reynolds number, lock-in is found when $U^* \leq 17.5$ Compared with previous cases in Figs. 9-14, the lock-in range here is larger, or with the increase of Re, the range of lock-in also increases. Figure 15 shows the motion amplitude Y_0^* and frequency ratio f^* in the lock-in region. At $U^* = 9.0$, $Y_{0max}^* = 0.94$ is the peak of motion amplitude in the lock-in region. There is a critical value, $U_{UL}^* = 10.7 - 10.8$, connecting upper and lower branches. Here a sudden drop occurs after the peak of motion amplitude, which is similar to that in the previous case of $Re = 5334$. After the sudden drop, the decrease of Y_0^* at $Re = 8890$ is slower than that at $Re = 5334$. From the analysis of the curves of Y_0^* in Figs. 9-15, it can be seen that none of them is similar to that in Fig. 6. It suggests that the behaviour in Fig. 6 is due to both U^* and Re, not just U^* as assumed. The effect of Re on free motion should be considered. Figure 16 shows the amplitude C_{L0} of lift coefficient in the lock-in region. It is interesting to see that at $Re = 8890$, the value of C_{L0} after the sudden drop is smaller than that with the same U^* at $Re = 5334$.

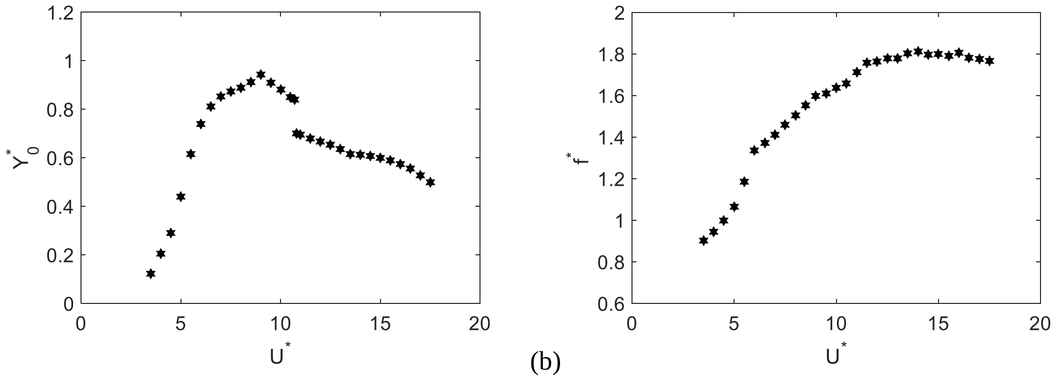

(a) (b)

Fig. 15. Motion amplitude and frequency ratio at $Re = 8890$.

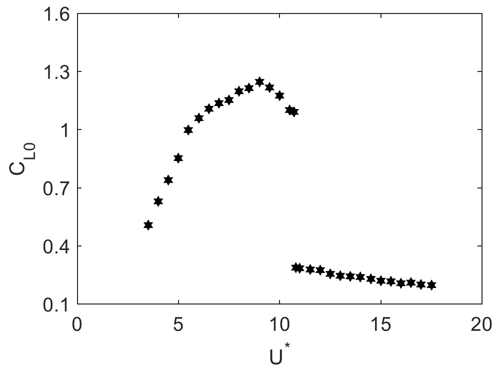

Fig. 16. Amplitude of lift coefficient at $Re = 8890$.

4.3. Body motion at U^*_{IU} and U^*_{UL} shown in Fig. 6

From the discussion on Section 4.2, it can be found that none of the Y^*_0 curves is similar to that in Fig. 6. It means that the behaviour in Fig. 6 is due to variations of both U^* and Re, not just U^* only, as assumed. In order to have some insight into the effect of Re on the jump of the Y^*_0 curve, we will run further simulations at values of Re corresponding to positions of two jumps in Fig. 6. The body mass and the damping ratio are the same as those used in Fig. 6, or $m^* = 0.935$ and $\zeta = 0.00502$.

The first jump in Fig. 6 occurs at $U_{IU}^* = 5.0 - 5.1$ (or $Re = 2540 - 2590$), and thus cases at $Re = 2540$ and $Re = 2590$ are chosen. Figure 17 shows the motion amplitude Y_0^* against U^* at $Re = 2540$ and 2590. It can be seen that for $Re = 2540$ and 2590, the curves of Y_0^* against U^* are very close and their shapes similar to that from the case with $Re = 1778$. There is still one critical value U_{IU}^* connecting the initial and upper branches. For $Re = 2540 - 2590$, U_{IU}^* is in the range from 5.0 to 5.1 similar to that of the first jump shown in Fig. 6. Figure 18 shows Y_0^* against Re at $U^* = 5.0$ and $U^* = 5.1$. It can be found that the curves of the Y_0^* at $U^* = 5.0$ and $U^* = 5.1$ are generally close. Both have a nearly vertical jump at $Re_{IU} = 2540 - 2590$, where there is an obvious difference between the two curves. It means that when $Re = 2540 - 2590$ and $U^* = 5.0 - 5.1$, the value of Y_0^* is sensitive to both the reduced velocity U^* and Reynolds number Re, or Y_0^* increases sharply with a small change of U^* or Re. Therefore, the first jump in Fig. 6 is very much related to variations of both U^* and Re.

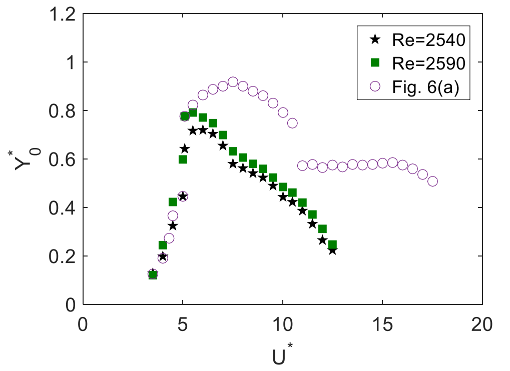

Fig. 17. Motion amplitude at $Re = 2540$ and $Re = 2590$ as well as that from Fig. 6(a).

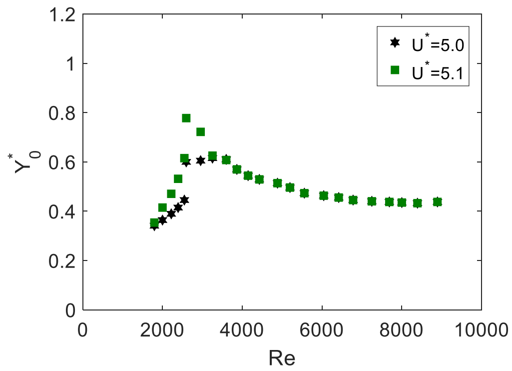

Fig. 18. Motion amplitude at $U^* = 5.0$ and $U^* = 5.1$.

Figure 19 shows Y_0^* against U^* at $Re = 5334$ and 5385 where the second jump in Fig. 6 occurs. The curve of Y_0^* at $Re = 5385$ is quite close to that at $Re = 5334$. These two curves have two branches, upper and lower branches connected by U_{UL}^*, which is approximately between 10.5 and 10.6. Even though both have only one nearly vertical jump, they are quite close to U_{UL}^* in Fig.6. Figure 20 shows Y_0^* against Re at $U^* = 10.5$ and $U^* = 10.6$. It can be seen that the curve of Y_0^* at $U^* = 10.5$ is quite different from that at $U^* = 10.6$. Based on the step of Reynolds number used in the calculation, there is only one branch of response in the Y_0^* curve at $U^* = 10.5$, while there are two branches, upper and lower branches connected by one nearly vertical drop at $U^* = 10.6$. Before the drop, the curve at $U^* = 10.6$ nearly coincides with that at $U^* = 10.5$ and both increase with Re. Y_0^* at $U^* = 10.6$ drops suddenly at a critical value of $Re = Re_{IL} = 5334$, while at $U^* = 10.5$ it continues to increase although the rate of increase is reduced. After that Y_0^* at $U^* = 10.6$ increases more rapidly and the curve then almost merges with that of $U^* = 10.5$. Thus, the difference between these two cases occurs only in a small region after the drop occurs in the case of $U^* = 10.6$. It suggests that when $Re = 5334 - 5385$ and $U^* = 10.5 - 10.6$, Y_0^* is sensitive to both the reduced velocity U^* and the Reynolds number Re. Therefore, the reason for the second jump shown in Fig. 6 is also related to both variations of U^* and Re. In such a case, the effect of Re on Y_0^* is significant and cannot be ignored.

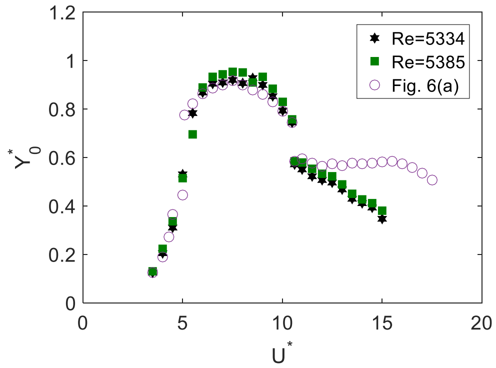

Fig. 19. Motion amplitude at $Re = 5334$ and $Re = 5385$.

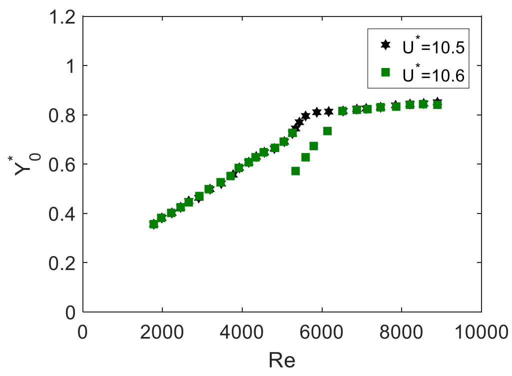

Fig. 20. Motion amplitude at $U^* = 10.5$ and $U^* = 10.6$.

5. Conclusions

The effect of Reynolds number on free motions of a circular cylinder in the lock-in region was investigated through a two-dimensional in-house code developed based on multi-block LBM together with LES as the turbulence model and IBM for the boundary condition. The focus has been on how the Reynolds number affects the motion amplitude curve against the reduced velocity, including branches and jumps. Simulations have been performed at the different Re in the range of $1524 - 12192$, with the body mass $m^* = 0.935$ and the damping ratio $\zeta = 0.00502$. From the results, the following conclusions can be drawn.

When Reynolds number Re is fixed, there are generally two branches in the curve of the motion amplitude Y_0^* against the reduced velocity U^*, instead of the usual three branches (Govardhan and Williamson, 2000) when Re changes with U^* from $Re = 1524$ $(U^* = 3.0)$ to $Re = 12192$ $(U^* = 24.0)$. The shape of Y_0^* curve varies when Re varies. At $Re = 1778$ there are only initial and upper branches, which are connected by U_{IU}^*. When approaching U_{IU}^* from the initial branch, Y_0^* increases rapidly or nearly vertically. When $Re \geq 3556$, there are only upper and lower branches linked by U_{UL}^*, and there is no U_{IU}^* where a nearly vertical increase of Y_0^* occurs. At $Re = 3556$,the motion amplitude Y_0^* drops steeply just after its peak, which corresponds to the start of the lower branch. At $Re = 5334$, in the upper branch, with the increase of U^*, Y_0^* increases first and then drops, and thus the sudden drop occurs away from the peak of Y_0^*. At $Re = 8890$, after the sudden drop, the decrease of Y_0^* becomes slower.

In the usual motion amplitude curve (Govardhan and Williamson, 2000), Re changes with U^*. When U^* approaches U^*_{IU} from the initial branch at U^*_{IU1} and from the upper branch at U^*_{IU2}, the corresponding Reynolds numbers are Re_{IU1} and Re_{IU2}. It is found that when Re is fixed at either Re_{IU1} or Re_{IU2}, the Y_0^* curves against U^* are very close to each other. While their Y_0^* curves in the initial branches are very similar to that in Govardhan and Williamson (2000) where Re changes with U^*, they are very different when $U^* > U^*_{IU2}$. When U^* is fixed at U^*_{IU1} or U^*_{IU2}, the two Y_0^* curves against Re are very different when Re is around Re_{IU1} to Re_{IU2}. Away from this region, the curves are close. Similarly at U^*_{UL}, corresponding to U^*_{UL1} and U^*_{UL2}, we have Re_{UL1} and Re_{UL2}. The two Y_0^* curves against U^* at $Re = Re_{UL1}$ and $Re = Re_{UL2}$ are very close. In the upper branch, they are very close to that in Govardhan and Williamson (2000), where Re changes with U^*, but very different in the lower branch. When U^* is fixed, the Y_0^* curve against Re has a jump around Re_{UL1} to Re_{UL2} at $U^* = U^*_{UL2}$, but is smooth at $U^* = U^*_{UL1}$. All these show that the effect of Re on the Y_0^* curve, including the branches, is far more complex than previously thought.

Appendix

The Chapman-Enskog expansion is used to get the relationship between the strain rate tensor $\bar{S}_{\alpha\beta}$ and the momentum flux tensor $\bar{Q}_{\alpha\beta}$ shown in Eq. (11). It assumes the following multi-scale expansion of time and space derivative in the small parameter ϵ,

$$\frac{\partial}{\partial t} = \epsilon \frac{\partial}{\partial t_1}, \tag{A.1}$$

$$\nabla = \epsilon \nabla^1 \text{ (or } \frac{\partial}{\partial \boldsymbol{x}} = \epsilon \frac{\partial}{\partial \boldsymbol{x}^1}\text{).} \tag{A.2}$$

Likewise, the distribution function is assumed as

$$f_i = f_i^{eq} + \epsilon f_i^1. \tag{A.3}$$

The equilibrium distribution function f_i^{eq} satisfies the following constraints (Wolf-Gladrow, 2000):

$$\sum_i f_i^{eq} = \rho, \tag{A.4}$$

$$\sum_i \boldsymbol{e}_i f_i^{eq} = \rho \bar{\boldsymbol{u}}, \tag{A.5}$$

and has the following properties (Aidun and Clausen, 2010)

$$\sum_i e_{i\alpha} e_{i\beta} f_i^{eq} = \rho \bar{u}_\alpha \bar{u}_\beta + \rho c_s^2 \delta_{\alpha\beta} = \rho \bar{u}_\alpha \bar{u}_\beta + \bar{p} \delta_{\alpha\beta} \qquad (\alpha, \beta = 1,2), \quad \text{(A.6)}$$

$$\sum_i e_{i\alpha} e_{i\beta} e_{i\gamma} f_i^{eq} = \rho c_s^2 \left(\bar{u}_\alpha \delta_{\beta\gamma} + \bar{u}_\beta \delta_{\alpha\gamma} + \bar{u}_\gamma \delta_{\alpha\beta} \right) \qquad (\alpha, \beta, \gamma = 1,2), \quad \text{(A.7)}$$

where $\bar{p} = \rho c_s^2$. In Eq. (A.6), the subscripts of α, β and γ of e_i and $\bar{\boldsymbol{u}}$ indicate that they are components of $\boldsymbol{e}_i$ and $\bar{\boldsymbol{u}}$ in α, β and γ directions with 1 and 2 indicating *x* and *y*, respectively. As f_i should also satisfy Eqs. (A.4) and (A.5), f_i^1 should then satisfy the following constraints:

$$\sum_i f_i^1 = 0, \ \sum_i \boldsymbol{e}_i f_i^1 = 0. \quad \text{(A.8)}$$

Through Taylor expansion with respect to δ_t, we rewrite Eq. (5) up to second order in δ_t

$$\left(\frac{\partial}{\partial t} + \boldsymbol{e}_i \cdot \nabla \right) f_i(\boldsymbol{x}, t) + \frac{\delta_t}{2} \left(\frac{\partial}{\partial t} + \boldsymbol{e}_i \cdot \nabla \right)^2 f_i(\boldsymbol{x}, t) = -\frac{1}{\tau_T \delta_t} \left[f_i(\boldsymbol{x}, t) - f_i^{eq}(\boldsymbol{x}, t) \right], \quad \text{(A.9)}$$

Here, δ_t is treated as the same order of ϵ. Substituting Eqs. (A.1) - (A.3) into Eq. (A.9), the equation of the first order in ϵ is written as

$$\left(\frac{\partial}{\partial t_1} + \boldsymbol{e}_i \cdot \nabla^1 \right) f_i^{eq} = -\frac{1}{\tau_T \delta_t} f_i^1. \quad \text{(A.10)}$$

The continuity equation to the first order in ϵ is obtained by summing Eq. (A.10) over the *i* velocities and using Eqs. (A.4), (A.5) and (A.8)

$$\frac{\partial \rho}{\partial t_1} + \nabla^1 \cdot (\rho \bar{\boldsymbol{u}}) = 0. \quad \text{(A.11)}$$

The momentum equation to the first order in ϵ is obtained by multiplying Eq. (A.10) by $\boldsymbol{e}_i$, summing it over the *i* velocities and using Eqs. (A.5), (A.6) and (A.8)

$$\frac{\partial \rho \bar{u}_\alpha}{\partial t_1} + \frac{\partial}{\partial x_\beta^1} \left(\rho \bar{u}_\alpha \bar{u}_\beta \right) = -\frac{\partial \bar{p}}{\partial x_\alpha^1}, \quad \text{(A.12)}$$

where the summation with respect to β is implied. The momentum flux tensor $\bar{Q}_{\alpha\beta}$ is

$$\bar{Q}_{\alpha\beta} = \sum_i e_{i\alpha} e_{i\beta} f_i^1. \quad \text{(A.13)}$$

Substituting Eq. (A.10) to Eq. (A.13), we have

$$\bar{Q}_{\alpha\beta} = -\tau_T \delta_t \left[\frac{\partial}{\partial t_1} \left(\sum_i e_{i\alpha} e_{i\beta} f_i^1 \right) + \frac{\partial}{\partial x_\gamma^1} \left(\sum_i e_{i\alpha} e_{i\beta} e_{i\gamma} f_i^1 \right) \right], \quad \text{(A.14)}$$

where the summation with respect to γ is implied. Inserting Eqs. (A.6) – (A.7) into Eq. (A.14), the following equation can be found

$$\bar{Q}_{\alpha\beta} = -\tau_T\delta_t\left\{\frac{\partial}{\partial t_1}\left(\rho\bar{u}_\alpha\bar{u}_\beta + \rho c_s^2\delta_{\alpha\beta}\right) + \frac{\partial}{\partial x_\gamma^1}\left[\rho c_s^2\left(\bar{u}_\alpha\delta_{\beta\gamma} + \bar{u}_\beta\delta_{\alpha\gamma} + \bar{u}_\gamma\delta_{\alpha\beta}\right)\right]\right\}. \quad \text{(A.15)}$$

$\frac{\partial}{\partial t_1}\left(\rho\bar{u}_\alpha\bar{u}_\beta + \rho c_s^2\delta_{\alpha\beta}\right)$ in Eq. (A.15) can be re-written as

$$\frac{\partial}{\partial t_1}\left(\rho\bar{u}_\alpha\bar{u}_\beta + \rho c_s^2\delta_{\alpha\beta}\right) = \bar{u}_\alpha\frac{\partial\rho\bar{u}_\beta}{\partial t_1} + \bar{u}_\beta\frac{\partial\rho\bar{u}_\alpha}{\partial t_1} - \bar{u}_\alpha\bar{u}_\beta\frac{\partial\rho}{\partial t_1} + c_s^2\frac{\partial\rho}{\partial t_1}\delta_{\alpha\beta}. \quad \text{(A.16)}$$

According to Eqs. (A.11) – (A.12), Eq. (A.16) can be written as

$$\frac{\partial}{\partial t_1}\left(\rho\bar{u}_\alpha\bar{u}_\beta + \rho c_s^2\delta_{\alpha\beta}\right) = -\bar{u}_\alpha c_s^2\frac{\partial\rho}{\partial x_\beta^1} - \bar{u}_\beta c_s^2\frac{\partial\rho}{\partial x_\alpha^1} - \bar{u}_\alpha\frac{\partial\rho\bar{u}_\beta\bar{u}_\gamma}{\partial x_\gamma^1} - \bar{u}_\beta\frac{\partial\rho\bar{u}_\alpha\bar{u}_\gamma}{\partial x_\gamma^1} + \bar{u}_\alpha\bar{u}_\beta\frac{\partial\rho\bar{u}_\gamma}{\partial x_\gamma^1} - c_s^2\frac{\partial\rho\bar{u}_\gamma}{\partial x_\gamma^1}\delta_{\alpha\beta}$$

$$= -\bar{u}_\alpha c_s^2\frac{\partial\rho}{\partial x_\beta^1} - \bar{u}_\beta c_s^2\frac{\partial\rho}{\partial x_\alpha^1} - \frac{\partial}{\partial x_\gamma^1}\left(\rho\bar{u}_\alpha\bar{u}_\beta\bar{u}_\gamma\right) - c_s^2\frac{\partial\rho\bar{u}_\gamma}{\partial x_\gamma^1}\delta_{\alpha\beta}. \quad \text{(A.17)}$$

$\frac{\partial}{\partial x_\gamma^1}\left[\rho c_s^2\left(\bar{u}_\alpha\delta_{\beta\gamma} + \bar{u}_\beta\delta_{\alpha\gamma} + \bar{u}_\gamma\delta_{\alpha\beta}\right)\right]$ in Eq. (A.15) can be re-written as

$$\frac{\partial}{\partial x_\gamma^1}\left[\rho c_s^2\left(\bar{u}_\alpha\delta_{\beta\gamma} + \bar{u}_\beta\delta_{\alpha\gamma} + \bar{u}_\gamma\delta_{\alpha\beta}\right)\right] = c_s^2\frac{\partial\rho\bar{u}_\gamma}{\partial x_\gamma^1}\delta_{\alpha\beta} + c_s^2\frac{\partial\rho\bar{u}_\beta}{\partial x_\alpha^1} + c_s^2\frac{\partial\rho\bar{u}_\alpha}{\partial x_\beta^1}$$

$$= c_s^2\frac{\partial\rho\bar{u}_\gamma}{\partial x_\gamma^1}\delta_{\alpha\beta} + \rho c_s^2\left(\frac{\partial\bar{u}_\alpha}{\partial x_\beta^1} + \frac{\partial\bar{u}_\beta}{\partial x_\alpha^1}\right) + c_s^2\bar{u}_\beta\frac{\partial\rho}{\partial x_\alpha^1} + c_s^2\bar{u}_\alpha\frac{\partial\rho}{\partial x_\beta^1}. \quad \text{(A.18)}$$

Substituting Eqs. (A.17) – (A.18) into Eq. (A.15), we have

$$\bar{Q}_{\alpha\beta} = -\tau_T\delta_t\left[\rho c_s^2\left(\frac{\partial\bar{u}_\alpha}{\partial x_\beta^1} + \frac{\partial\bar{u}_\beta}{\partial x_\alpha^1}\right) - \frac{\partial}{\partial x_\gamma^1}\left(\rho\bar{u}_\alpha\bar{u}_\beta\bar{u}_\gamma\right)\right]. \quad \text{(A.19)}$$

Here as in Qian and Orszag (1993), $\frac{\partial\rho\bar{u}_\alpha\bar{u}_\beta\bar{u}_\gamma}{\partial x_\gamma^1}\Big/\left[\rho c_s^2\left(\frac{\partial\bar{u}_\alpha}{\partial x_\beta^1} + \frac{\partial\bar{u}_\beta}{\partial x_\alpha^1}\right)\right] = O(M^2)$, and thus if $M^2 \ll 1$, the second term in Eq. (A.19) can be neglected, which is consistent with the order of accuracy of Eq. (5) for the Navier-Stokes equations. We have

$$\bar{Q}_{\alpha\beta} = -2\tau_T\delta_t\rho c_s^2\bar{S}_{\alpha\beta}. \quad \text{(A.20)}$$

This gives

$$\bar{S}_{\alpha\beta} = -\frac{1}{2\tau_T\delta_t\rho c_s^2}\bar{Q}_{\alpha\beta} = \sum_i e_{i\alpha}e_{i\beta}\left(f_i - f_i^{eq}\right). \quad \text{(A.21)}$$

Acknowledgements

The first author is sponsored by the scholarship of China Scholarships Council, to which she is most grateful. The authors also gratefully acknowledge financial support from the Lloyd's Register Foundation (LRF). The LRF helps to protect life and property by supporting engineering-related education, public engagement and the application of research.

References

Aidun, C.K., Clausen, J.R., 2010. Lattice-Boltzmann method for complex flows. Annual Review of Fluid Mechanics 42, 439-472.

Bearman, P.W., 1984. Vortex shedding from oscillating bluff bodies. Annual Review of Fluid Mechanics 16, 195-222.

Bearman, P.W., 2011. Circular cylinder wakes and vortex-induced vibrations. Journal of Fluids and Structures 27, 648-658.

Blevins, R.D., 1990. Flow-induced Vibrations. Van Nostrand Reinhold, New York.

Cercignani, C., 1998. The Boltzmann Equation and Its Application. Spring, New York.

Chen, S., 2009. A large-eddy-based lattice Boltzmann model for turbulent flow simulation. Applied Mathematics and Computation, 215, 591-598.

Chen, S., Doolen, G., 1998. Lattice Boltzmann method for fluid flows. Annual Review of Fluid Mechanics 30, 329–364.

Chen, Z., Shu, C., Tan, D., 2018. Immersed boundary-simplified lattice Boltzmann method for incompressible viscous flows. Physics of Fluids 30, 053601.

Dorogi, D., Baranyi, L., 2020. Identification of upper branch for vortex-induced vibration of a circular cylinder at Re = 300. Journal of Fluids and Structuures 98: 103135.

Garcia, S., 2007. The lid-driven square cavity flow: from stationary to time periodic and chaotic. Communications in Computational Physics 2, 900-932.

Ghia, U., Ghia, K.N., Shin, C.T., 1982. High-Re solutions for incompressible flow using the Navier-Stokes equations and a multigrid method. Journal of Computational Physic 48, 387-411.

Govardhan, R., Williamson, C.H.K., 2000. Modes of vortex formation and frequency response of a freely vibrating cylinder. Journal of Fluid Mechanics 420, 85-130.

Govardhan, R., Williamson, C.H.K., 2006. Defining the 'modified Griffin plot' in vortex-induced vibration: revealing the effect of Reynolds number using controlled damping. Journal of Fluid Mechanics 561, 147-180.

He, X., Luo, L., 1997. Lattice Boltzmann model for the incompressible Navier-Stokes equation. Journal of Statistical Physics 88 927-944.

Hou, S., Sterling, J., Chen, S., Doolen, G.D., 1996. A lattice Boltzmann subgrid model for high Reynolds number flows. Fields Institute Communication 6,151–66.

Hou, S., Zou, Q., Chen, S., Doolen, G.D., Cogley, A.C., 1995. Simulation of cavity flow by the lattice Boltzmann method. Journal of Computational Physics 118, 329-347.

Jiao, H., Wu, G.X., 2018a. Analysis of fluctuating force acting on two cylinders in different arrangements through Lattice Boltzmann Method. Journal of Fluids and Structures 82, 101-120.

Jiao, H., Wu, G.X., 2018b. Free vibration predicted using forced oscillation in the lock-in region. Physics of Fluids 30, 113601.

Khalak, A., Williamson, C.H.K., 1997. Fluid forces and dynamics of a hydroelastic structure with very low mass dan damping. Journal of Fluids and Structures 11, 973-982.

Klamo, J.T., Leonard, A., Roshko, A., 2005. On the maximum amplitude for a freely vibrating cylinder in cross-flow. Journal of Fluids and Structures 21, 429-434.

Kumar, S., Novrose, Mittal, S., 2016. Lock-in in forced vibration of a circular cylinder. Physics of Fluids 28, 113605.

Norberg, C., 2003. Fluctuating lift on a circular cylinder: review and new measurements. Journal of Fluids and Structures 17, 57-96.

Pigazzini, R., Contento, G., Martini, S., Puzzer, T., Morgut, M., Mola, A., 2018. VIV analysis of a single elastically-mounted 2D cylinder: parameter identification of a single-degree-of-freedom multi-frequency model. Journal of Fluids and Structures 78, 299-313.

Peskin, C.S., 2002. The immersed boundary method. Acta Numerica 11, 479-517.

Qian, Y.H., Orszag, S.A., 1993. Lattice BGK models for the Navier-Stokes equation: nonlinear deviation in compressible regime. Europhysics Letters 21(3), 255-259.

Skop, R.A., Griffin, O.M., 1973. A model for the vortex-excited resonant response of bluff cylinders. Journal of Sound and Vibration 27(2), 225-233.

Skop, R.A., Griffin, O.M., 1975. On a theory for the vortex-excited oscillations of flexible cylindrical structures. Journal of Sound and Vibration 41(3), 263-274.

Smagorinsky, J., 1963. General circulation experiments with the primitive equations: I. The basic experiments. Monthly Weather Review 91, 99-164.

Sumer, B.M., Fredsoe, J., 1997. Hydrodynamics around Cylindrical Structures. World Scientific, Singapore.

Wanderley, J.B.V., Soares, L.F.N., 2015. Vortex-induced vibration on a two-dimensional circular cylinder with low Reynolds number and low mass-damping parameter. Ocean Engineering 97, 156-164.

Wanderley, J.B.V., Sphaier, S.H., Levi, C.A., 2018. A number investigation of vortex induced vibration on an elastically mounted rigid cylinder. In: 27th International Conference on Offshore Mechanics and Arctic Engineering-OMAE, ASME, Lisboa.

Williamson, C.H.K., 1996. Vortex dynamics in the cylinder wake. Annual Review of Fluid Mechanics 28, 477-539.

Williamson, C.H.K., Govardhan, R., 2004. Vortex-induced Vibrations. Annual Review of Fluid Mechanics 36, 413-455.

Wolf-Gladrow, D.A., 2000. Lattice-gas Cellular Automata and Lattice Boltzmann Models: An Introduction. Springer, New York.

Yu, D., Mei, R., Shyy, W., 2002. A multi-block lattice Boltzmann method for viscous fluid flows. International Journal for Numerical Methods in Fluids 39, 99-120.

Yu, H., Girimaji, S.S., Luo, L., 2005. DNS and LES of decaying isotropic turbulence with and without frame rotation using lattice Boltzmann method. Journal of Computational Physics 209, 599-616.